Comprehensive Study of Biomass Particle Combustion

Hong Lu,* Warren Robert, Gregory Peirce, Bryan Ripa, and Larry L. Baxter

Chemical Engineering Department, Brigham Yong University, Provo, Utah 84602

Received January 5, 2008. Revised Manuscript Received March 13, 2008

This investigation provides a comprehensive analysis of entrained-flow biomass particle combustion processes. A single-particle reactor provided drying, pyrolysis, and reaction rate data from poplar particle samples with sizes ranging from 3 to 15 mm. A one-dimensional particle model simulates the drying, rapid pyrolysis, gasification, and char oxidation processes of particles with different shapes. The model characterizes particles in three basic shapes (sphere, cylinder, and flat plate). With the particle geometric information (particle aspect ratio, volume, and surface area) included, this model can be modified to simulate the combustion process of biomass particles of any shape. The model also predicts the surrounding flame combustion behaviors of a single particle. Model simulations of the three shapes agree nearly within experimental uncertainty with the data. Investigations show that spherical mathematical approximations for fuels that either originate in or form aspherical shapes during combustion poorly represent combustion behavior when particle size exceeds a few hundred microns. This includes a large fraction of the particles in both biomass and black liquor combustion. In particular, composition and temperature gradients in particles strongly influence the predicted and measured rates of temperature rise and combustion, with large particles reacting more slowly than is predicted from isothermal models.

1. Introduction

During the past two decades, interest in renewable energy sources has increased due to at least two driving forces: (1) the increasing concern about the environmental impact of fossil and nuclear energy; and (2) the increasing anxiety regarding the security and longevity of fossil fuel.

The threat of regional and global climate change (global warming) may require significant reduction in the emissions of greenhouse gases—most notably CO_2. One potential strategy for reducing such emissions is the replacement of fossil fuels with renewable biomass fuels. Renewable fuels can be essentially CO_2-neutral if derived from sustainable cultivation practices with minimal fossil fuel usage. Unlike fossil fuels, biomass fuels can be renewable and CO_2-neutral in the sense that the CO_2 generated by biomass utilization recycles from the atmosphere to the plants that replace the fuel, closing the carbon loop on a short time scale. If the biomass is renewably produced (as is generally the case in developed nations), there is little net increase in atmospheric CO_2 content. Since most biomass, including essentially all biomass residue, decays in any case, sometimes producing methane and other decomposition products that greatly exceed the potency of CO_2 as greenhouse gases, use of biomass residues as fuel has the potential of actually decreasing greenhouse gas impacts, not just being neutral.[1]

Di Blasi[2] investigated the influences of physical properties on biomass devolatilization. A detailed particle energy and mass transport model predicted the effects of density, thermal conductivity, permeability to gas flow, and specific heat capacity.

The author concluded that variations in physical properties mainly affect reactivities of secondary reactions of tar vapors and the conversion time for conversion in a thermally thick regime (intraparticle heat transfer control). Biomass density and the char thermal conductivity exhibit the highest sensitivity.

Miller and Bellan[3] performed a parametric investigation of reactor temperature, heating rate, porosity, initial particle size, and initial temperature effects on char yields and conversion times using a spherically symmetric particle pyrolysis model. An increase in heating rate decreased both the char yield and the conversion time for both cellulose and wood. Additionally, both char yield and conversion time are increasing functions of initial particle size.[3] The char yield increase arises from secondary reactions between tar vapor and solids in the particle and the lower temperature heat-up.

Baxter and Robinson[4] applied engineering models of kinetics, heat transfer, and mass transfer to predict the effects of particle size and density, shape, internal temperature gradients, and composition. The results of mass loss history of biomass particles were compared with data collected from several highly instrumented furnaces. Drying and devolatilization were found to be primarily heat-transfer controlled whereas oxidation was found to be primarily mass-transfer controlled for most biomass of practical concern. In their later research, they found devolatilization removes most of the mass. Under rapid, high-temperature pyrolysis conditions, up to 95 wt % (daf) of the mass is released during devolatilization, significantly more than ASTM tests.

The effects of particle size, reactor heating rate, and final reactor temperature were theoretically and experimentally

* To whom correspondence should be addressed. Telephone: 1-949-330-8970. Fax: 1-949-330-8994. E-mail: honglu@research.ge.com. Current address: 18A Mason, Irvine, CA 92618.

(1) Mann, M. A Comparison of the Environmental Consequences of Power from Biomass, Coal, and Natural Gas; 2001. (cited; available from http://www.nrel.gov/analysis/pdfs/2001/novdc.pdf.
(2) Di Blasi, C. Influences of Physical Properties on Biomass Devolatilization Characteristics. *Fuel* **1997**, *76*, 957–964.

(3) Miller, R. S.; Bellan, J. Analysis of Reaction Products and Conversion Time in the Pyrolysis of Cellulose and Wood Particles. *Combust. Sci. Technol.* **1996**, *119*, 331–373.
(4) Bharadwaj, A.; Baxter, L. L.; Robinson, A. L. Effects of intraparticle heat and mass transfer on biomass devolatilization: Experimental results and model predictions. *Energy Fuels* **2004**, *18*, 1021–1031.

investigated by Di Blasi.[5] Similar results were obtained: large particle size increases char yields; higher heating rates result in higher volatile yields and lower char yields. This researech indicates three main regimes of solid-fuel pyrolysis: the thermally thick (diameter = 0.625 cm), the thermally thin (diameter = 0.04 cm), and the pure kinetic regime. The pure kinetic limit involves only particles at least 1 order of magnitude smaller than those allowing conversion in the thermally thin regime, except at very low temperatures.

As for particle shape, a spherical particle shape is usually assumed in modeling work for convenience. Other particle shapes have been considered. Jalan and Srivastava[6] studied pyrolysis of a single cylindrical biomass particle, and particle size and heating rate effects were investigated. In Horbaj's model[7] and Liliddahl's model,[8] a particle geometric factor was introduced to account for the particle shape, which can deal with a prism (or slab), a cylinder (or rod), and a sphere.

In 2000, Janse and Westerhout[9] simulated the flash pyrolysis of a single wood particle. To investigate the influence of particle shape, simulations included spherical, cylindrical, and flat particles. Results show that spherical particles react most quickly compared to other particle shapes if the characteristic size is taken as the minimum particle dimension. The higher surface-area-to-volume ratio of spherical particles on this basis explains this observation; flat particles react most slowly. In the work reported later in this document, the characteristic dimension is taken as the spherical-equivalent diameter: the diameter of a sphere with the same volume/mass as the aspherical particle. As will be shown, using the spherical-equivalent diameter results in the opposite trend—spherical particles react most slowly. There is no inconsistency in these results, just a difference in basis of comparison. At small particle diameters (typically less than 200 μm), the rate of reaction becomes dominant and the different particle shapes exhibit nearly equal conversion times. Flat particles seem to yield less gas and more char. This research also showed that an increase in particle diameter (or conversion time) caused no change in bio-oil yield, a slight decrease in gas yield, and a slight increase in char yield. This might be due to the low reactor temperature (surface temperature 823 K) they used to simulate this process.

Coal char reactivity and oxidation processes enjoy an extensive literature developed during the last decades. Char, either from coal or biomass, is usually considered to be mainly composed of carbon, containing far fewer heteroatoms (O, H, S, and N) than the fuels from which they derive but nonetheless retaining some heteroatoms and in any case having structures and reactivity very different from graphite. In this sense, the chemical structure of biomass char is similar to coal char, but large physical differences exist between them, such as density, thermal conductivity, porosity, surface area, and particle shape and size.

Mermoud and his co-workers[10] collected experimental steam gasification reactivity data with beech char and compared with model predictions. The usual homogeneous or shrinking core particle models produced unacceptable results and that only the assumption of thermal equilibrium between the particle and the surrounding gas is valid for a model at bed scale.

With birch wood chars obtained from a free-fall tubular reactor and a thermobalance, Chen et al.[11] studied char reactivity with carbon dioxide and steam in the thermobalance. Reaction rates of the char depend strongly on particle temperature history during char formation. Chars obtained from rapid pyrolysis possessed higher reactivity (2.3−2.4 times higher) in the reaction with carbon dioxide or steam compared with chars from slow pyrolysis. In other words, kinetic rates of char increase with increasing particle heating rate during the thermal decomposition process.

The reactivity of two kinds of biomass chars from Southern pine and switchgrass was investigated by Wornat et al.[12] Results showed that, at early stages of char conversion, both of the chars were quite reactive. However, their reactivity decreased somewhat during char conversion as more reactive carbon is preferentially depleted and the inorganic constituents of the chars underwent physical and chemical transformations that render them less catalytically active. They also found that even with small biomass char particles (75−106 μm), the irregular morphologies and their wide range of burning rates made a more rigorous and detailed kinetic analysis quite difficult.

Results from Di Blasi and co-workers[13] indicate that in the kinetically controlled regime (low temperature ~873 K) and under nonisothermal conditions (10, 20−80 K/min heating rate), the reactivities (dm/dt) of three biomass chars (wheat straw, olive husks, and grape residues) increased with conversion first, reaching a maximum, and decreased or remained constant, then increased again as a function of conversion. A one-step global model interprets the mass loss curves in their work with conversion-dependent parameters. At low temperatures in a TGA, Adanez and his co-workers[14] determined combustion reactivities of five biomass chars with a combined method, with similar results.

A recent paper[15] investigated the combustion characteristics of moving and suspended biomass particles both experimentally and mathematically. It was found that isothermal particle assumption is no longer valid when particle size exceeds 150−200 μm.

Detailed single biomass particle combustion data, including particle mass loss and temperature history as functions of time, is rarely reported in the above literature. This investigation summarizes experimental drying, devolatilization conversion, and char oxidation rates for poplar particles in a single particle reactor, as well as a model that predicts these data nearly within

(5) Di Blasi, C. Kinetics and Heat Transfer Control in the Slow and Flash Pyrolysis of Solids. *Ind. Eng. Chem. Res.* **1996**, *35*, 37–46.

(6) Jalan, R. K.; Srivastava, V. K. Studies on Pyrolysis of a Single Biomass Cylindrical Pellet Kinetic and Heat Transfer Effects. *Energy Convers. Manage.* **1999**, *40* (5), 467–494.

(7) Horbaj, P. Model of the Kinetics of Biomass Pyrolysis. *Drevarsky Vyskum* **1997**, *42* (4), 15–23.

(8) Liliedahl, T.; Sjostrom, K. Heat transfer controlled pyrolysis kinetics of a biomass slab, rod or sphere. *Biomass Bioenergy* **1998**, *15* (6), 503–509.

(9) Janse, A. M. C.; Westerhout, R. W. J.; Prins, W. Modelling of Flash Pyrolysis of a Single Wood Particle. *Chem. Eng. Process.* **2000**, *39*, 239–252.

(10) Mermoud, F.; Golfier, F.; Salvador, S.; Van de Steene, L.; Dirion, J. L. Experimental and numerical study of steam gasification of a single charcoal particle. *Combust. Flame* **2006**, *145*, 59–79.

(11) Chen, G.; Yu, Q.; Sjostrom, K. Reactivity of Char from Pyrolysis of Birch Wood. *J. Anal. Appl. Pyrolysis* **1997**, *40−41*, 491–499.

(12) Wornat, M. J.; Hurt, R. H.; Davis, K. A.; Yang, N. Y. C. Single-Particle Combustion of Two Biomass Chars. In *Twenty-Sixth Symposium (International) on Combustion*; The Combustion Institute: Pittsburgh, PA, 1999.

(13) Di Blasi, C.; Buonanno, F.; Branca, C. Reactivities of Some Biomass Chars in Air. *Carbon* **1999**, *37*, 1227–1238.

(14) Adanez, J.; de Diego, L. F.; Garcia-Labiano, F.; Abad, A.; Abanades, J. C. Determination of Biomass Char Combustion Reactivities for FBC Applications by a Combined Method. *Ind. Eng. Chem. Res.* **2001**, *40*, 4317–4323.

(15) Yang, Y. B.; Sharifi, V. N.; Swithenbank, J.; Ma, L.; Darvell, L. I.; Jones, J. M.; Pourkashanian, M.; Williams, A. Combustion of a Single Particle of Biomass. *Energy Fuels* **2008**, *22*, 306–316.
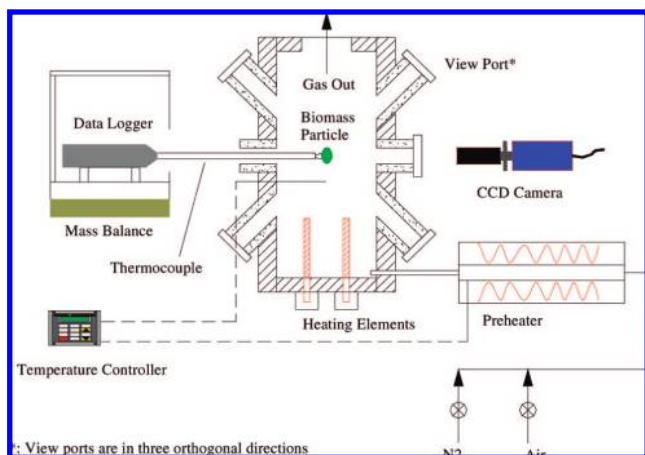
Figure 1. Single-particle reactor schematic diagram.

their experimental uncertainty, providing detailed descriptions of particle mass and temperature change for a single particle during combustion.

2. Experimental Method

A single-particle reactor[16] is used to investigate the drying, devolatilization, and char oxidation/gasification behaviors of biomass particles. Figure 1 schematically illustrates the experimental facility for the single particle combustion study.

Poplar particles with two regular shapes, cylinder and near-sphere, were obtained by cutting 9.5 mm diameter poplar dowel rod to different aspect ratios: 1.0 for near-spherical and 4.0 for cylindrical particles. Moisture content of the samples is usually about 6%. To study the drying behavior of biomass particles, samples with higher moisture contents were also prepared by soaking in water for different periods and kept in closed sample bottles.

Single biomass particles suspended on a type B or type K thermocouple and connected to a wireless data logger, from PACE Scientific, provided internal temperature data at a speed of 20 Hz. The data logger, thermocouple, and the biomass particle were placed on top of a balance to provide dynamic mass loss data. A small hole of about the same size of the thermal couple wire (∼0.25 mm) was drilled through the center the particle for thermocouple suspension. Mass loss data were collected and recorded with the balance with a resolution of 0.1 mg. The imaging system and optical pyrometer recorded the physical changes and surface temperature distribution of the biomass particle. The data logger, balance, and imaging system collect data simultaneously. All equipment and devices are synchronized within 1 s. For particle devolatilization processes, particle surface temperature was also measured by a thermocouple. To reduce the influence of thermal conduction on surface temperature measurement, a shallow and narrow groove was cut on the particle surface and the wire was buried next to the surface.

This single-particle reactor produces experimental data, including mass loss, and surface and center temperature, as functions of time for poplar dowel particles during drying, pyrolysis, and char oxidation/gasification processes.

3. Particle Mathematical Model

As a biomass particle hovers in the single-particle reactor with air as carrier gas, it exchanges energy by both radiation and convection and by chemical reactions. The biomass particle undergoes the following processes: drying, devolatilization, volatiles combustion, char gasification, and char oxidation. These
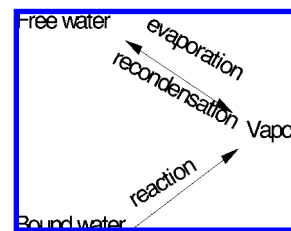

Figure 2. Moisture drying scheme.

processes may occur sequentially or simultaneously, depending on particle properties and reactor conditions.

Mechanisms of Drying, Devolatilization, and Char Gasification and Oxidation. Moisture in biomass occurs in two forms: free water and bound water.[17] Moisture content above the fiber saturation point (FSP) is free water, that is, exists in liquid form in pores and cells. Below the FSP, moisture is bound water, that is, exists as moisture physically or chemically bound to surface sites or as hydrated species. The average FSP is about 30%,[17] which is the weight of water in the wood as a percentage of the weight of oven-dry wood (essentially water content on a dry basis). Traditionally, the forest products industries express moisture on this basis, so that 100% moisture means essentially half of the mass is water. Nuclear magnetic resonance (NMR) can determine free water and bound water contents.[18] Free moisture vaporizes from both the internal and external surface at a rate determined by the surface saturated vapor pressure, the partial pressure of vapor in the gas phase. Bound water does not vaporize in a manner similar to free moisture but rather is released as a result of chemical reactions releasing bound hydrates and similar processes. Four basic methods, including a thermal model, equilibrium model, and chemical reaction model, describe wood drying under combustion heat fluxes.[19] In this model, a mass transfer expression, with the difference between equilibrium vapor pressure and vapor partial pressure as the driving force, describes both the evaporation of free water and recondensation of vapor. The evaporation rate of bound water proceeds by a chemical reaction rate expression.[20] Figure 2 illustrates the drying scheme of moisture. Poplar particles used in the single-particle reactor usually have 6% moisture content, which is categorized as bound water. Samples with higher moisture content, up to 50%, were also prepared and used to collect free-water drying process data and validate the drying model.

Devolatilization or pyrolysis involves heating of raw biomass components or organic materials in the absence of oxidizer, thermal degradation of the biomass components, mass transport of the devolatilization products by advection and diffusion, and escape of products at the surface of the particle. A few authors distinguish between pyrolysis and devolatilization, with the former occurring in a neutral or reducing environment and the latter in an oxidizing environment. Most particles thermally decompose within a volatile cloud (reducing environment) even

(16) Ip, L.-T. Comprehensive black liquor droplet combustion studies. *Chemical Engineering*; Brigham Young University: Provo, UT, 2005.
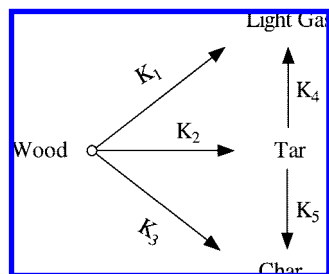
(17) Forest Products Laboratory United States Department of Agriculture Forest Service. Physical Properties and Moisture Relations of Wood. In *Wood Handbook: Wood as an Engineering Material*; Forest Products Society: Madison, WI, 1999; Chapter 3, pp 3−5.

(18) Guzenda, R.; Olek, W. Identification of free and bound water content in wood by means of NMR relaxometry. In *12th International Symposium on Nondestructive Testing of Wood*; Sopron: Budapest, Hungary, 2000.

(19) Bryden, K. M.; Hagge, M. J. Modeling the combined impact of moisture and char shrinkage on the pyrolysis of a biomass particle. *Fuel* **2003**, *82*, 1633–1644.

(20) Chan, W.-C.R.; Kelbon, M.; Krieger, B. B. Modeling and experimental verification of physical and chemical processes during pyrolysis of a large biomass particle. *Fuel* **1985**, *64* (11), 1505–1513.

Figure 3. Two-stage wood pyrolysis model.[21]

Table 1. Light Gas Composition Produced during Devolatilization

components	H_2	CO	CO_2	H_2O	light hydrocarbon
mass fraction	0.109	0.396	0.209	0.249	0.127

when the overall environment is oxidizing, making this distinction somewhat ambiguous. The two terms are used interchangeably in this document, consistent with most of the literature. The two-stage wood pyrolysis kinetics model, shown in Figure 3, is chosen for this particle model since it is capable of predicting the product yields and distribution variations with temperature and heating rate which are significantly influenced by particle shape and size.

The volatile yield from pyrolysis includes a complex mixture and more than 100 hydrocarbons were found.[22–24] Pyrolysis product distribution depends strongly on reactor temperature, heating rate, residence time, and mass transfer velocity and pressure.[24] This complex mixture mainly consists of CO, CO_2, H_2O, H_2, light hydrocarbons, and heavy hydrocarbons. The first five components are classified as light gas, and the last one as tar. For the light gas composition, reaction kinetics from Thunman et. al[25] predict wood pyrolysis volatile components in this model, with the mass fraction of each species listed in Table 1. To simplify the combustion behaviors of volatiles, the light hydrocarbon and heavy hydrocarbon are lumped together as hydrocarbons in the current investigation, and the lumped hydrocarbon molecule is $C_6H_{6.2}O_{0.2}$, consistent with published results.[25] In this model, hydrocarbon combustion in the gas phase occurs through a one-step global reaction according to the approximate composition of hydrocarbon, even though the combustion chemistry of a simple gas could be a complex phenomenon.[26] The reaction mechanism and kinetic parameters for the hydrocarbon combustion are based on the recommendations of Smoot and Smith.[27]

Char gasification and oxidation include five classic heterogeneous and homogeneous reactions, indicated as reactions 8–12 in Table 2. In coal char combustion, reaction 8 is

described by both first- and half-order expressions.[28,29] Biomass char reactivity literature is less substantial than that for coal char, but some report that biomass char has slightly higher reactivity than that of coal.[12,13,30,31] The oxidation rate of biomass char varies between a half- and first-order, as demonstrated by Janse et al.[32] According to Bryden's[33] analysis, lignite's kinetic parameters are used for wood char oxidation since wood char more closely resembles lignite than other coal types. The oxidation kinetic mechanisms make this model more robust, but in practice oxidation occurs mostly under diffusion-controlled conditions, in which case the details of the kinetics are immaterial.

Parameters describing chemical reactions and phase changes, together with their corresponding rate expressions during drying, devolatilization, and char oxidation processes, appear in Table 2.

Arrhenius expressions describe the temperature dependence of the kinetic rate coefficients for reactions 1–5 and 7–13, as indicated in eqs 1 and 2.

In reactions 1–5, 7, and 11–13

$$k_i = A_i \exp\left(-\frac{E_i}{RT}\right) \qquad (1)$$

and in reactions 8–10,

$$k_i = A_i T \exp\left(-\frac{E_i}{RT}\right) \qquad (2)$$

The literature-based kinetic parameters for wood pyrolysis vary widely. They are usually measured at low to moderate temperature (usually <900 K). No high-temperature kinetic data for the two-stage scheme appear in the literature. Font et al.[35] presented kinetic data for the three primary reactions that are found to be comparable to what Nunn et al.[36] reported for the single reaction kinetic data for hardwood in the high-temperature range (573–1373 K). Font et al.'s results are used in this model for sawdust samples, and Wagenaar's[37] pine wood pyrolysis kinetics data are applied for poplar samples. The pre-exponential factors, activation energy, and standard heats of reaction for all the reactions used in this model appear in Table 3.

Heat, Mass, and Momentum Transfer Control Equations. The following assumptions allow tractable mathematical combustion model development:

(21) Di Blasi, C. Heat, Momentum and Mass Transport through a Shrinking Biomass Particle Exposed to Thermal Radiation. *Chem. Eng. Sci.* **1996**, *51* (7), 1121–1132.

(22) Evans, R. J.; Milne, T. A. Molecular Characterization of the Pyrolysis of Biomass. 1. Fundamentals. *Energy Fuels* **1987**, *1*, 123–137.

(23) Evans, R. J.; Milne, T. A. Molecular Characterization of the Pyrolysis of Biomass. 2. Applications. *Energy Fuels* **1987**, *1*, 311–319.

(24) Demirbas, A. Hydrocarbons from Pyrolysis and Hydrolysis Processes of Biomass. *Energy Sources* **2003**, *25*, 67–75.

(25) Thunman, H.; Niklasson, F.; Johnsson, F.; Leckner, B. Composition of Volatile Gases and Thermochemical Properties of Wood for Modeling of Fixed or Fluidized Beds. *Energy Fuels* **2001**, *15*, 1488–1497.

(26) Warnatz, J. Hydrocarbon oxidation high-temperature chemistry. *Pure Appl. Chem.* **2000**, *72* (11), 2101–2110.

(27) Smoot, L. D.; Smith, P. J. *Coal Combustion and Gasification*; Plenum Press: New York, 1985.

(28) Smith, K. L.; Smoot, L. D.; Fletcher, T. H.; Pugmire, R. J. The structure and reaction processes of coal. In *The Plenum Chemical Engineering Series*; Luss, D., Ed.; Plenum Press: New York, 1994.

(29) Brewster, B. S.; Hill, S. C.; Radulovic, P. T.; Smoot, L. D. *Fundamentals of Coal Combustion for Clean and Efficient Use*; Smoot, L. D. , Ed.; Elsevier Applied Science Publishers: London, 1993; Vol. 20.

(30) Blackham, A. U.; Smoot, L. D.; Yousefi, P. Rates of oxidation of millimetre-sized char particles: simple experiments. *Fuel* **1994**, *73* (4), 602–612.

(31) Evans, D. H.; Emmons, H. W. Combustion of wood charcoal. *Fire Res.* **1977**, (1), 57–66.

(32) Janse, A. M. C.; de Jonge, H. G.; Prins, W.; van Swaaij, W. P. M. Combustion kinetics of char obtained by flash pyrolysis of pine wood. *Ind. Eng. Chem. Res.* **1998**, *37*, 3909–3918.

(33) Bryden, K. M. *Computational Modeling of Wood Combustion*; Mechanical Engineering Department, University of Wisconsin-Madison: Madison, WI, 1998.

(34) Hautman, D. J.; Dryer, L.; Schug, K. P.; Glassman, I. A multiple-step overall kinetic mechanism for the oxidation of hydrocarbons. *Combust. Sci. Technol.* **1981**, *25*, 219–235.

(35) Font, F.; Marcilla, A.; Verdu, E.; Devesa, J. Kinetics of the pyrolysis of almond shells and almond shells impregnated with CoCl2 in a fluidized bed reactor and in a pyroprobe 100. *Ind. Eng. Chem. Res.* **1990**, *29*, 1846–1855.

(36) Nunn, T. R.; Howard, J. P.; Longwell, T.; Peters, W.A. Product compositions and kinetics in the rapid pyrolysis of sweet gum hardwood. *Ind. Eng. Chem., Process Des. Dev.* **1985**, *24*, 836–844.

(37) Wagenaar, B. M.; Prins, W.; Van Swaaij, W. P. Flash pyrolysis kinetics of pine wood. *Fuel Process. Technol.* **1993**, *36*, 291.

Table 2. Chemical Reactions, Phase Change and Rate Expressions

reaction index	reaction description	rate expression	ref
1	biomass → light gas	$r_1 = \partial\rho_B/\partial t = k_1\rho_B$	
2	biomass → tar	$r_2 = \partial\rho_B/\partial t = k_2\rho_B$	
3	biomass → char	$r_3 = \partial\rho_B/\partial t = k_3\rho_B$	
4	tar → light gas	$r_4 = \partial\rho_G/\partial t = \varepsilon k_4\rho_g Y_T$	
5	tar → char	$r_5 = \partial\rho_C/\partial t = \varepsilon k_5\rho_g Y_T$	
6	$H_2O(l,free) \leftrightarrow H_2O(g)$	$r_6 = \partial\rho_{fw}/\partial t = s_a(\rho_{fw}/\rho_{fw}^0)h_{m,pore}(\rho_v^{sat} - Y_V\rho_g)$	
7	$H_2O(l,bound) \rightarrow H_2O(g)$	$r_7 = \partial\rho_{bw}/\partial t = k_7\rho_{bw}$	20
8	$C + {}^1/_2O_2 \rightarrow CO$	$r_8 = \partial C_{O_2}/\partial t = s_{a,char}[\rho_C/(\rho_C + \rho_B + \rho_A)]k_8\varepsilon C_{O_2}$	31
9	$C + CO_2 \rightarrow 2CO$	$r_9 = \partial C_{CO_2}/\partial t = s_{a,char}[\rho_C/(\rho_C + \rho_B + \rho_A)]k_9\varepsilon C_{CO_2}$	29
10	$C + H_2O \rightarrow CO + H_2$	$r_{10} = \partial C_{H_2O}/\partial t = s_{a,char}[\rho_C/(\rho_C + \rho_B + \rho_A)]k_{10}\varepsilon C_{H_2O}$	29
11	${}^1/_2O_2 + CO \rightarrow CO_2$	$r_{11} = \partial C_{CO}/\partial t = k_{11}C_{CO}C_{O_2}^{0.25}C_{H_2O}^{0.5}$	34
12	$H_2 + {}^1/_2O_2 \rightarrow H_2O$	$r_{12} = \partial C_{H_2}/\partial t = k_{12}C_{H_2}C_{O_2}^{1.42}$	34
13	$C_6H_{6.2}O_{0.2} + 2.9O_2 \rightarrow 6CO + 3.1H_2$	$r_{13} = \partial C_{HC}/\partial t = k_{13}C_{HC}^{0.5}C_{O_2}$	27

Table 3. Kinetic Data and Heats of Reaction

reaction index	A (1/s)	E (kJ/mol)	ref	temp range (K)	ΔH (kJ/kg)	ref
1 (hardwood sawdust)[a]	1.52×10^7	139.2	35	733−878	−418	20
1 (poplar)[a]	1.11×10^{11}	177	37	573−873		
2 (hardwood sawdust)[a]	5.85×10^6	119	35	733−878	−418	20
2 (poplar)[a]	9.28×10^9	149	37	573−873		
3 (hardwood sawdust)[a]	2.98×10^3	73.1	35	733−878	−418	20
3 (poplar)[a]	3.05×10^7	125	37	573−873		
4	4.28×10^6	107.5	38	−	42	39
5	1.0×10^5	107.5	40	−	42	39
6	5.13×10^{10}	88	19	−	−2440	19
8	0.658 (m/(s·K))	74.8	31	−	9212	19
9	3.42 (m/(s·K))	130	29	−	14370	41
10	3.42 (m/(s·K))	130	29	−	10940	41
11	$10^{12.35}$	167	34	−	10110	41
12	$10^{12.71}$	171.3	34	−	120900	41
13	$10^{4.32} \times T \times 0.3P$	80.2	27	−	41600	33

[a] These are all one-step kinetics for pyrolysis.

• a transient one-dimensional model sufficiently describes particle behavior;

• local thermal equilibrium exists between the solid and gas phase in the particle, so internal temperatures and their gradients are the same for the solid and gas;

• gases behave as ideal gases, including both relationships between pressure, temperature, and specific volume and dependence of heat capacity on temperature only;

• particle aspect ratios and shapes do not change during devolatilization, though size does change dynamically. The shape and aspect ratio is a simplifying assumption for this case but not required by the model in general;

• heat and mass transfer at particle boundaries increase relative to that of a sphere by the ratio of the particle surface to that of a volume-equivalent sphere—a close approximation to results from more detailed analyses for similarly sized particles.

Particle shapes represented by a parameter n include a sphere ($n = 2$), cylinder ($n = 1$), and flat plate ($n = 0$). The biomass particle initially contains inert gas or air. In total, 12 species appear in the model: biomass, char, free water, bound water, ash, CO, CO_2, H_2O, H_2, O_2, lumped hydrocarbon (tar), and inert gas. The mass conservation of each species, the momentum,

and the total energy equations, as well as the initial and boundary conditions, appear as eqs 3–33.

The biomass temporal mass balance contains three consumption terms, one each for the reactions to light gas, tar, and char, where all terms in this expression and most terms in subsequent expressions depend on both time and position.

$$\frac{\partial\rho_B}{\partial t} = S_B \tag{3}$$
$$\text{where } S_B = -(r_1 + r_2 + r_3)$$

Similarly, the char temporal mass balance contains five source terms, one from the conversion of biomass to char and one for the char yield from the secondary reactions of tar, as well as the gasification and oxidation reactions.

$$\frac{\partial\rho_C}{\partial t} = S_C$$

where

$$S_C = r_3 + r_5 - r_8\frac{2M_C}{M_{O_2}} - r_9\frac{M_C}{M_{CO_2}} - r_{10}\frac{M_C}{M_{H_2O}} \tag{4}$$

The temporal free-water mass balance contains a loss associated with conversion to vapor and a source term associated with water vapor readsorption into the particle, as determined by reaction 6 in Table 2. The free water also migrates due to the pressure gradient in the liquid phase.[42,43] The migration flux is based on Darcy's law for this porous media, which is propor-

(38) Liden, C. K.; Berruti, F.; Scott, D. S. A kinetic model for the production of liquids from the flash pyrolysis of biomass. *Chem. Eng. Commun.* **1988**, *65*, 207–221.

(39) Koufopanos, C. A.; Papayannakos, N.; Maschio, G.; Lucchesi, A. Modelling of the Pyrolysis of Biomass Particles. Studies on Kinetics, Thermal and Heat Transfer Effects, *Can. J. Chem. Eng.* **1991**, *69* (4), 907–915.

(40) Di Blasi, C. Analysis of convection and secondary reaction effects within porous solid fuels undergoing pyrolysis. *Combust. Sci. Technol.* **1993**, *90*, 315–340.

(41) Turns, S. R. *An Introduction to Combustion: Concepts and Applications*, 2nd ed.; McGraw-Hill: New York, 2000.

(42) Ouelhazi, N.; Arnaud, G.; Fohr, J. P. A Two-dimensional study of wood plank drying. The effect of gaseous pressure below boiling point. *Transp. Porous Media* **1992**, *7* (1), 39–61.

(43) De Paiva Souza, M. E.; Nebra, S. A. Heat and mass transfer model in wood chip drying. *Wood Fiber Sci.* **2000**, *32* (2), 153–163.

tional to the total liquid pressure gradient. The total liquid pressure is equal to the pressure of the gas phase minus the capillary pressure of the gas−liquid interface. An effective free water diffusivity $D_{\text{eff,fw}}$ is derived to describe the migration with Fick's law applied based on the Darcy's law results.[43] Equation 5 gives the mass balance for free water. The mass transfer coefficient of vapor in the pore $h_{\text{m,pore}}$, which appears in the evaporation rate reaction 6, is determined by eq 6.[44]

$$\frac{\partial \rho_{\text{fw}}}{\partial t} = \frac{1}{r^n}\frac{\partial}{\partial r}\left(r^n D_{\text{eff,fw}}\frac{\partial \rho_{\text{fw}}}{\partial r}\right) + S_{\text{fw}}$$

where

$$S_{\text{fw}} = -r_6 \tag{5}$$

$$h_{\text{m,pore}} = 3.66 \times D_{\text{eff,H}_2\text{O}}/d_{\text{pore\_hydraulic}} \tag{6}$$

Bound water has similar migration in the radial direction but responds to a chemical potential gradient rather than a pressure/concentration gradient, and the phase change follows the chemical reaction r7, shown in Equation 7.

$$\frac{\partial \rho_{\text{bw}}}{\partial t} = \frac{1}{r^n}\frac{\partial}{\partial r}\left(r^n D_{\text{eff,bw}}\frac{\partial \rho_{\text{bw}}}{\partial r}\right) + S_{\text{bw}}$$

where

$$S_{\text{bw}} = -r_7 \tag{7}$$

Several different correlations describe diffusivities of free water and bound water;[42,43,45] Olek et al.'s method is applied in this investigation. The diffusivities of both free water and bound water are direction dependent, and the diffusivity in the axial direction is larger than that in the tangential direction. Details appear at the end of this section in the physical property list.

The ash in the particle is assumed to be inert, so that ash density is constant for nonshrinking/swelling particle

$$\frac{\partial \rho_A}{\partial t} = 0 \tag{8}$$

$$\frac{\partial}{\partial t}\varepsilon\rho_g Y_i + \frac{1}{r^n}\frac{\partial}{\partial r}(r^n\varepsilon\rho_g Y_i u) = \frac{1}{r^n}\frac{\partial}{\partial r}\left(r^n\varepsilon D_{\text{eff},i}\rho_g\frac{\partial Y_i}{\partial r}\right) + S_i \tag{9}$$

The conservation equations for all gas-phase components (CO, CO_2, H_2O, O_2, H_2, HC, and inert gas) include temporal and spatial gradients, convection, and source terms as follows. Source terms for each gas-phase species appear below:

$$S_{\text{CO}_2} = r_{11}\frac{M_{\text{CO}_2}}{M_{\text{CO}}} - r_9 + (r_1 + r_4)\alpha_{\text{CO}_2} \quad S_{\text{CO}} = r_8\frac{2M_{\text{CO}}}{M_{\text{O}_2}} + r_9\frac{2M_{\text{CO}}}{M_{\text{CO}_2}} +$$

$$r_{10}\frac{M_{\text{CO}}}{M_{\text{H}_2\text{O}}} + r_{13}\frac{6M_{\text{CO}}}{M_{\text{HC}}} - r_{11} + (r_1 + r_4)\alpha_{\text{CO}} \quad S_{\text{O}_2} = -r_8 -$$

$$r_{11}\frac{M_{\text{O}_2}}{2M_{\text{CO}}} - r_{12}\frac{M_{\text{O}_2}}{2M_{\text{H}_2}} - r_{13}\frac{2.9M_{\text{O}_2}}{M_{\text{HC}}} \quad S_{\text{H}_2} = (r_1 + r_4)\alpha_{\text{H}_2} +$$

$$r_{10}\frac{M_{\text{H}_2}}{M_{\text{H}_2\text{O}}} - r_{12} + r_{13}\frac{3.1M_{\text{H}_2}}{M_{\text{HC}}} \quad S_{\text{H}_2\text{O}} = (r_1 + r_4)\alpha_{\text{H}_2\text{O}} + r_6 + r_7 -$$

$$r_{10} + r_{12}\frac{M_{\text{H}_2\text{O}}}{M_{\text{H}_2}} \quad S_{\text{HC}} = r_2 + (r_1 + r_4)\alpha_{\text{HC}} - r_4 - r_5 - r_{13} \quad S_{\text{I}} = 0 \tag{10}$$

The overall gas-phase continuity equation results from the sum of these species and has the form

$$\frac{\partial}{\partial t}\varepsilon\rho_g + \frac{1}{r^n}\frac{\partial}{\partial r}(r^n\varepsilon\rho_g u) = S_g$$

where

$$S_g = r_1 + r_2 - r_5 + r_6 + r_7 + r_8\frac{2M_{\text{C}}}{M_{\text{O}_2}} + r_9\frac{M_{\text{C}}}{M_{\text{CO}_2}} + r_9\frac{M_{\text{C}}}{M_{\text{H}_2\text{O}}} \tag{11}$$

The gas-phase velocity in the particle obeys a Darcy law type expression

$$u = -\frac{\eta}{\mu}\frac{\partial p}{\partial r}$$

where

$$p = \frac{\rho_g R_g T}{M_{\text{W}}} \tag{12}$$

The gas mixture is ideal, and the permeability, η, is a mass-weighted function of the individual solid-phase permeabilities:

$$\eta = \frac{\rho_{\text{B}}}{\rho_{\text{B,0}}}\eta_{\text{B}} + \left(1 - \frac{\rho_{\text{B}}}{\rho_{\text{B,0}}}\right)\eta_{\text{C}} \tag{13}$$

The energy conservation equation includes the following terms:

$$\frac{\partial}{\partial t}\left[\sum_i \rho_i\hat{H}_i + \sum_k \rho_k\hat{H}_k + \varepsilon\rho_g\sum_j Y_j\hat{H}_j\right] +$$
$$\frac{1}{r^n}\frac{\partial}{\partial r}\left[r^n\varepsilon\rho_g u\sum_j Y_j\hat{H}_j\right] = \frac{1}{r^n}\frac{\partial}{\partial r}\left(r^n K_{\text{eff}}\frac{\partial T}{\partial r}\right) +$$
$$\frac{1}{r^n}\frac{\partial}{\partial r}\left[r^n\left(\rho_g\varepsilon\sum_j D_{\text{eff},j}\frac{\partial Y_j}{\partial r}\hat{H}_j + D_{\text{eff},k}\frac{\partial \rho_k}{\partial r}\hat{H}_k\right)\right] \tag{14}$$

where $\hat{H}_l = \hat{H}_{l,\text{f}}^0 + \int_{T_0}^T C_{p,l}(T)\,\mathrm{d}T$, l is any species involved, i = any species or component in the solid phase, j = any species or component in the gas phase, and k = free water and bound water.

This form of the energy equation relates to standard theoretical analyses[46] for multicomponent systems. In eq 14, the first term represents the energy accumulation, the second term represents energy convection, the third term (first term after the equality) accounts for conduction heat transfer, and the last term accounts for energy associated with species diffusion in the gas phase and the liquid phase. The last term generally contributes only negligibly to the overall energy balance and is commonly justifiably ignored. No heats of reaction appear in the expression since the energy balances total enthalpy (both phases) and is not written in terms of temperature or separate particle and gas phases. Heats of reaction only become apparent when separately modeling the particle and gas phases or using temperature instead of enthalpy. Radiation between the gas and solid phase in the particle is incorporated into the effective conductivity, as explained below.

The effective diffusivity of gas species in the particle can be calculated by the parallel pore[47] model, as shown in eq 15.

$$D_{\text{eff}} = \frac{D\varepsilon}{\tau}$$

where

(44) Incropera, F. P.; Dewitt, D. P. *Fundamentals of Heat and Mass Transfer*, 4th ed.; John Wiley & Sons: New York, 1996.

(45) Olek, W.; Perre, P.; Weres, J. Inverse analysis of the transient bound water diffusion in wood. *Holzforschung* **2005**, *59* (1), 38–45.

(46) Bird, R. B.; Stewart, W. E.; Lightfoot, E. N. *Transport Phenomena*, 2nd ed.; John Wiley & Sons, Inc.: New York, 2002.

(47) Wheeler, A. *Advances in Catalysis*; Academic Press: New York, 1951; p 250.

$$\frac{1}{D} = \frac{1}{D_{AB}} + \frac{1}{D_K} \tag{15}$$

An identical diffusivity for each species and Fickian diffusion assumptions, as implied here, avoid the complexity of more formal multicomponent diffusion calculations.

The effective particle thermal conductivity includes radiative and conductive components with some theoretical basis[48,49] and with empirical verification for wood.[9]

$$K_{eff} = K_{cond} + K_{rad} \tag{16}$$

where the particle structure is assumed to be close to the upper limit for thermal conductivity; that is, it is assumed to have high connectivity in the direction of conduction

$$K_{cond} = \varepsilon K_{gas} + (1 - \varepsilon)\left[\frac{\rho_B}{\rho_{B,0}}K_B + \left(1 - \frac{\rho_B}{\rho_{B,0}}\right)K_C\right]$$

$$K_{gas} = \sum_j Y_j K_j \tag{17}$$

and where radiation contributes approximately to the third power of the temperature

$$K_{rad} = \frac{\varepsilon \sigma T^3 d_{pore}}{\omega} \tag{18}$$

The emissivity of the particle is the mass-weighted result of each solid component: biomass, ash, and char. A volume-weighted emissivity might be more appropriate, but it is not available in this case: all components are assumed to occupy the same total volume.

$$\omega = \frac{\rho_A}{\sum \rho_i}\omega_A + \frac{\rho_B}{\sum \rho_i}\omega_B + \frac{\rho_C}{\sum \rho_i}\omega_C \tag{19}$$

The thermal conductivity of a wet biomass particle is based on Ouelhazi's[42] empirical correlation which states that the effective thermal conductivity is a function of temperature and moisture contents. Thermal conductivity is anisotropic, with the value in the fiber direction 2.5 times that in the transversal direction. An average value of both the fiber and transveral directions is adopted in this paper. Details of the thermal conductivity of the wet biomass particle appear at the end of this section.

Initial conditions depend on experimental conditions for a nonreacting particle. That is, at $t = 0$

$$\begin{aligned}
p(t=0, r) &= p_{atm} \\
T(t=0, r) &= 300 \text{ K (typically)} \\
u(t=0, r) &= 0 \\
Y_I(t=0, r) &= 1 \\
Y_{i(j,k)}(t=0, r) &= 0
\end{aligned} \tag{20}$$

Boundary conditions at the particle center reflect the spherical symmetry, that is, at $r = 0$

$$\begin{aligned}
\frac{\partial p}{\partial r}^{t,r=0} &= 0 \\
u_{t,r=0} &= 0 \\
\frac{\partial T}{\partial r}^{t,r=0} &= 0 \\
\frac{\partial Y_{i(j,k)}}{\partial r}_{t,r=0} &= 0
\end{aligned} \tag{21}$$

During biomass particle combustion, the flame surrounding the particle may affect particle surface temperature by heat generated in the flame that feeds back to the surface and further heats the particle. The model describes both the particle domain and the boundary layer domain, which includes the flame during combustion. The boundary layer flame, as with many other model features, can be turned on or off during simulation.

If the boundary layer domain is off, boundary conditions at the particle outer surface depend on external conditions of pressure and heat and mass flux:

$$\begin{aligned}
p(t, r=r_p) &= p_{atm} \\
\frac{\partial Y_{i(j,k)}}{\partial r}_{r=r_p} &= \theta_m h_m R_{SA}(Y_{i(j,k),\infty} - Y_{i(j,k),S}) \\
k_{eff}\frac{\partial T}{\partial r}_{r=r_p} &= \theta_T h_T R_{SA}(T_f - T) + R_{SA}\omega\sigma(T_w^4 - T^4)
\end{aligned} \tag{22}$$

where θ_m and θ_T represent the blowing factors[46] for mass transfer and heat transfer, respectively. RSA represents the exterior surface area ratio, which is the surface area of the particle divided by the characteristic surface area, as follows:

$$R_{SA} = SA/(4\pi R_p^2) \quad R_{SA} = SA/(4\pi R_p^2 AR) \quad R_{SA} = SA/(4R_p^2 AR^2) \tag{23}$$

for spheres, cylinders, and flat plates, respectively.

Each shape employs heat transfer coefficients developed for that particular shape. Correlations suitable for random particle orientation during flight appear in the literature for some particles.[50] Where such a model is not available, the characteristic length of the particle is the arithmetic average length of the particle. For near-spherical particles, Masliyah's prolate spheroid model[50] provides a suitable correlation, as indicated in eq 24.

$$Nu = 1.05 + 0.6Re^{0.65}Pr^{0.33} \tag{24}$$

Cylinders at low Reynolds numbers adopt the correlation of Kurdyumov[51] (eq 25).

$$Nu = W_0(Re)Pr^{0.33} + W_1(Re) \tag{25}$$

The heat transfer coefficient for a flat plate appears in Equation 26.

$$Nu = 0.644Re^{0.5}Pr^{0.343} \tag{26}$$

Mass transfer coefficient calculations are analogous to heat transfer correlations respectively for each specific particle shape.

If the boundary layer domain is turned on, the boundary conditions assume those in the bulk flow (indicated by infinity subscripts), as shown in eq 27.

$$\begin{aligned}
p_{r>=r_p} &= p_{atm} \\
Y_{i(j,k)r=r_p+BLT_m} &= Y_{i(j,k),\infty} \\
T_{r=r_p+BLT_T} &= T_\infty
\end{aligned} \tag{27}$$

where BLT_m and BLT_T are boundary layer thickness of mass transfer and heat transfer, respectively. The determination of these two types of boundary layer thicknesses is straightforward if the particle stays in inert carrier gas (nitrogen). A linear method is adopted to approximate the boundary layer thicknesses, as illustrated below.

(48) Robinson, A. L.; Buckley, S. G.; Baxter, L. L. Thermal Conductivity of Ash Deposits 1: Measurement Technique. *Energy Fuels* **2001**, *15*, 66–74.

(49) Robinson, A. L.; Buckley, S. G.; Yang, N. Y. C.; Baxter, L. L. Thermal Conductivity of Ash Deposits 2: Effects of Sintering. *Energy Fuels* **2001**, *15*, 75–84.

(50) Masliyah, J. H.; Epstein, N. Numerical solution of heat and mass transfer from spheroids in steady axisymmetric flow. *Prog. Heat Mass Transfer* **1972**, *6*, 613–632.

(51) Kurdyumov, V. N.; Fernandez, E. Heat transfer from a circular cylinder at low Reynolds numbers. *J. Heat Transfer, Trans. ASME* **1998**, *120* (1), 72–75.

The linear approximation assumes that the gradient at the particle surface can be approximated by an algebraic difference:

$$\frac{dY}{dr} \approx \frac{\Delta Y}{\Delta r} = \frac{Y_\infty - Y_S}{\text{BLT}_\text{m}} \tag{28}$$

The mass transfer at the particle surface is also correlated with the empirical mass transfer correlation:

$$D_\text{AB}\frac{dY}{dr} = h_\text{m}\theta_\text{m}(Y_\infty - Y_\text{s}) \tag{29}$$

where the mass transfer coefficient can be calculated by

$$Sh = \frac{d_\text{P}h_\text{m}}{D_\text{AB}} \tag{30}$$

So, substituting eqs 29 and 30 into eq 28 leads to the boundary layer thickness for mass transfer:

$$\text{BLT}_\text{m} = \frac{d_\text{P}}{Sh \cdot \theta_\text{m}} \tag{31}$$

Similarly, the boundary layer thickness of heat transfer based on the linear approximation is

$$\text{BLT}_\text{T} = \frac{d_\text{P}}{Nu \cdot \theta_\text{T}} \tag{32}$$

When the particle is surrounded by air instead of nitrogen, a flame forms in the boundary layer. The resulting temperature and species concentration distributions in the boundary layer may influence the boundary layer thickness, making it different from that calculated based on the heat and mass transfer correlations illustrated above. The determination of the exact boundary layer thickness for such a burning particle with surrounding flame could be complicated due to bulk flow convection (slip velocity) in the reactor axial direction and the off-gases from the particle. A two-dimensional model might be needed to predict the exact boundary layer thickness. In this investigation, eqs 31 and 32 are applied to determine the thickness of the boundary layer, where flame is formed during combustion. Model predictions agree well with experimental data.

To simplify momentum conservation, constant boundary-layer pressure is assumed, equal to the atmospheric pressure. The secondary cracking reactions of tar and soot formation in the boundary layer are neglected, although combustion reactions are included. A radiation energy flux has to be added to the energy equation for the node on the particle physical surface due to the radiation between the particle surface and reactor wall.

Particle shrinking or swelling during drying, pyrolysis, and char gasification and oxidation depends on the following empirical correlation:

$$\frac{v}{v^0} = 1 + x_\text{M}(\beta_\text{M} - 1.0) + x_\text{B}(\beta_\text{B} - 1.0) + x_\text{C}(\beta_\text{C} - 1.0) \tag{33}$$

which can be used to describe both shrinking and swelling behaviors of a burning solid particle or droplet. In eq 33, v is the current control volume of each cell and v^0 initial control volume of each cell; x_m, x_B, x_C are conversion of moisture, biomass, and char; β_M is the swelling/shrinking factor of moisture drying, 0.9 for wood particle drying shrinking; β_B is the swelling/shrinking factor of biomass devolatilization, 0.9 for wood particle shrinking; β_C is the shrinking factor of char burning, 0.0 for constant char density shrinking (conceptually

consistent with the typically external diffusion controlled oxidation rates).

The density change of each species in the solid phase is determined by the following equation due to volume change.

$$\frac{\partial \rho_i}{\partial t} = S_i - \frac{\rho_i}{v}\frac{\partial v}{\partial t}, \tag{34}$$

where i = char, ash, and biomass.

The physical properties of the biomass particles significantly affect the heat and mass transfer rates.[2,52] In this work, temperature-dependent heat capacity correlations are used for all species. The heat capacity of biomass and char adopt the model suggested by Merrick.[53] Gronli et al.[54] suggested a correlation for tar heat capacity, which is based on some typical pyrolysis tar components (closely related to benzene). All physical properties appear in Table 4.

This one-dimensional complete mathematical model for the combustion of a single biomass particle includes a set of partial differential equations (PDEs) to describe the mass, heat, and momentum transfer in the particle domain and the flame layer domain. A control volume method[58] reformulates these differential equations into a set of algebraic equations amenable to computer simulation. A fully implicit scheme is applied for the transient term in the energy conservation equation, each species conservation equation, and momentum equation; the convection and diffusion/conduction terms are solved by the power law scheme; control volume faces occur midway between the grid points; a staggered grid is used for velocity component; the SIMPLE algorithm is applied for the momentum transfer to calculate the flow field.

4. Results and Discussion

The single-particle combustion model comparisons with mass loss data and particle temperature data collected on the single-particle reactor provide model validation below. Then, a series of model predictions with different levels of complexity illustrate the necessity of such a sophisticated structure model for biomass particle combustion modeling. Finally, more model investigations and experimental data are presented and discussed.

Single-Particle Combustion Model Validation. Combustion experiments in the single-particle reactor validate the combustion model by comparisons of particle surface temperature, internal temperature, and mass loss during drying, devolatilization, and char oxidation.

The single-particle reactor wall temperature is not uniform in the axial direction due to reactor configurations, so an average wall temperature determined at the location of the particle is

(52) Raveendran, K.; Ganesh, A.; Khilart, K. C. Influence of Mineral Matter on Biomass Pyrolysis Characteristics. *Fuel* **1995**, *74* (12), 1812–1822.

(53) Merrick, D. Mathematical models of the thermal decomposition of coal - 2. Specific heats and heats of reaction. *Fuel* **1983**, *62* (5), 540–546.

(54) Gronli, M. G.; Melaaen, M. C. Mathematical model for wood pyrolysis - comparison of experimental measurements with model predictions. *Energy Fuels* **2000**, *14*, 791–800.

(55) DIPPR. Design Institute of Physical Property Data. http://dippr.by-u.edu/index.asp [cited; available from: http://dippr.byu.edu/index.asp.

(56) Lee, C. K.; Chaiken, R. F.; Singer, J. M. Charring pyrolysis of wood in fires by laser simulation. *Symp. (Int.) Combust, 16th, MIT, Aug 15−20* **1976**, 1459–1470.

(57) Kansa, >E. J.; Perlee, H. E.; Chaiken, R. F. Mathematical model of wood pyrolysis including internal forced convection; 1977, *29*, 3, 311−324.

(58) Patankar, S. V. Numerical Heat Transfer and Fluid Flow. In *Series in Computational Methods in Mechanics and Thermal Sciences*; Taylor & Francis: New York, 1980.

Table 4. Physical Properties of Biomass Particles

property	value	ref
wood density ρ_B	650 kg/m^3 (sawdust), 580 kg/m^3 (poplar particle)	
porosity ϵ	0.4	
emissivity ω	$\omega_A = 0.7$, $\omega_B = 0.85$, $\omega_C = 0.95$	
permeability η (Darcy)	$\eta_B = 1$, $\eta_C = 100$	54
thermal conductivity k (W/(m·K))	k_j, gas species thermal conductivity is calculated based on DIPPR correlations	55
	$k_A = 1.2$	
	wet biomass in tangential direction:	42
	if $C_w > 0.4$:	
	$k_B = (9.32 \times 10^{-2} + 6.5 \times 10^{-3}C_w)(1 + 3.65 \times 10^{-3}(T - 273.15))(0.986 + 2.695C_w)$	
	if $C_w \leq 0.4$:	
	$k_B = (0.129 - 4.9 \times 10^{-2}C_w)(1 + (2.05 + 4C_w) \times 10^{-3}(T - 273.15))(0.986 + 2.695C_w)$	
	thermal conductivity in axial direction is 2.5 times of the tangential one	
	$k_C = 0.071$	56
biomass particle specific surface area S_a (m^2/m^3)	9.04×10^4	BET
char particle specific surface area $S_{a,char}$ (m^2/m^3)	1.0×10^6	BET
pore size d_{pore} (m)	3.2×10^{-6}	BET
hydraulic pore diameter, $d_{pore,hydraulic}$	$d_{pore,hydraulic} = 4.0\varepsilon/S_a(1.0 - \varepsilon)$	
molecular weight M (kg/kmol)	$M_T = 145$	9
viscosity μ (Pa·s)	$\mu_{gas} = 3 \times 10^{-5}$ for all gas species	57
diffusivity DAB (m^2/s)	DAB $= 3.0 \times 10^{-5}$ for all gas species	9
		45

$$D_{eff,bw} = D_0 \exp\left(\frac{-E_b}{RT}\right)$$

where C_{bw} is bound water content, $D_0 = 5 \times 10^{-5}$ m/s, $E_b = a_1 - a_2 C_{bw}$ $a_1 = 31030$ J/mol, and $a_2 = 10000$ J/mol

		43

$$D_{eff,fw} = 6.1 \times 10^3 \left(\frac{k_{fw}}{\eta_{fw}}\right) \varepsilon^{0.61} \left(\frac{\rho_s C_{fw}}{\rho_{fw}}\right)$$

$$k_{fw} = \begin{cases} 0, & \text{if } \left(\frac{\rho_s C_{fw}}{\varepsilon \rho_{fw}}\right) \leq S_{ir} \\ k_{fw}^\Phi \left(1 - \cos\frac{\pi}{2}\left(\frac{(\rho_s C_{fw}/\varepsilon \rho_{fw}) - S_{ir}}{1 - S_{ir}}\right)\right), & \text{if } \left(\frac{\rho_s C_{fw}}{\varepsilon \rho_{fw}}\right) > S_{ir} \end{cases}$$

$S_{ir} = 0.1$, irreducible saturation, $k_{fw}^\Phi = 3.0 \times 10^{-15}$ m^2

heat capacity C_p (J/(kg·K))		53

$$C_{p,B} = \left(\frac{1000R_g}{7.72}\right)\left[g\left(\frac{380}{T}\right) + 2g\left(\frac{1800}{T}\right)\right]$$

| | | 53 |

$$C_{p,C} = \left(\frac{1000R_g}{11.3}\right)\left[g\left(\frac{380}{T}\right) + 2g\left(\frac{1800}{T}\right)\right]$$

where

$$g(x) = \frac{x^2 e^x}{(e^x - 1)^2}$$

$C_{p,T} = -100 + 4.4 \times T - 0.00157 \times T_2$ 54

$C_{p,j}$ of all gas species except hydrocarbon is based on DIPPR database correlations   55

used in the model as the reactor wall temperature. Both a type K thermocouple and the imaging pyrometer measure this temperature. The thermocouple reading was 1303 K and the average pyrometer measurement was 1276 K. The imaging pyrometer data are taken as the wall temperature here. A type K thermocouple monitors the center gas temperature. The actual gas temperature was corrected for radiative and other losses from the thermocouple bead based on the wall temperature, bulk gas velocity, and the thermocouple bead size. This resulted in a gas temperature of 1050 K.

Particle Devolatilization. Data for a near-spherical particle (d_p = 11 mm) with aspect ratio of 1.0 and a moisture content of 6.0 wt %, including mass loss, center and surface temperature during pyrolysis, appear with model predictions in Figures 4 and 5. The nominal conditions of this experiment include a

reactor wall temperature of 1273 K and gas temperature of 1050 K. All the following validation experiments used the same conditions.

The particle mass loss and particle surface temperature predictions generally agree with experimental data except that the measured particle center temperature increases faster than the model predictions at the beginning. This discrepancy likely arises from thermal conduction through the thermocouple wire, as discussed later. In principle, the measured particle surface temperature and center temperature should reach the same value at the end of pyrolysis, but a small discrepancy exists in differences in thermocouple bead size and shape and ash coating on the center temperature bead. A more detailed discussion of the features of these data
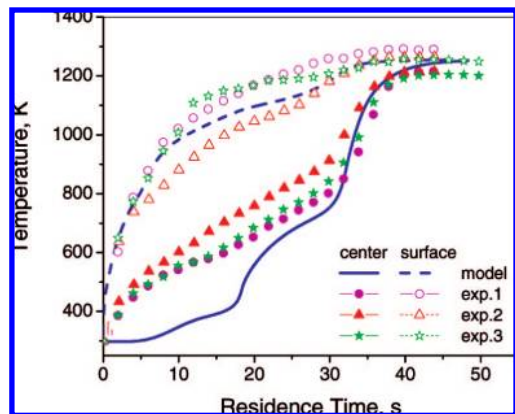
Figure 4. Temperature of near-spherical particle during pyrolysis in nitrogen (d_p = 9.5 mm, AR = 1.0, MC = 6 wt %, T_w = 1276 K, T_g = 1050 K).
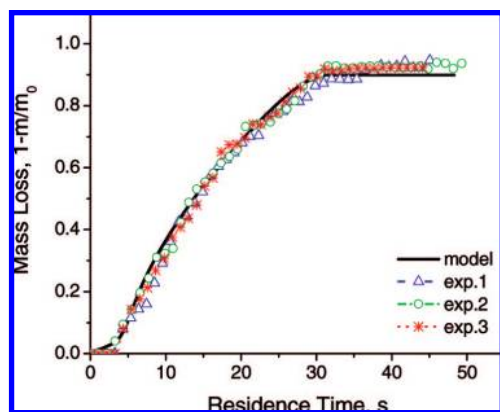

Figure 6. Temperature comparison of a cylindrical particle during pyrolysis in nitrogen (d_p = 9.5 mm, AR = 4.0, MC = 6 wt %, T_w = 1276 K, T_g = 1050 K).

Figure 5. Mass loss of near-spherical particle during pyrolysis in nitrogen (d_p = 9.5 mm, AR = 4.0, MC = 40 wt %, T_w = 1276 K, T_g = 1050 K).

Figure 7. Mass loss comparison of a cylindrical particle during pyrolysis in nitrogen (d_p = 9.5 mm, AR = 4.0, MC = 6 wt %, T_w = 1276 K, T_g = 1050 K).

appears after discussion of the potential cause of the discrepancy in the center temperature data.

To determine the thermocouple lead wire impact on the measured center temperature, a second experiment at the same conditions used a cylindrical particle of the same diameter but with aspect ratio of 4.0. Two thermocouples monitored the center temperature, one passing axially and a second passing radially through the particle. The axial thermocouple should be less impacted by heat conduction through the leads since the particle provides some insulation from the radiation and buoyancy-driven bulk-flow convection. In Figure 6, lines 1 and 2 are particle center temperatures measured in the radial direction; lines 3 and 4 are results measured in axial direction. As indicated, the center temperature measured in the radial direction increases much faster than that measured in axial direction at the beginning, indicating that the thermocouple wire conduction influences initial center temperature measurements. The model prediction for the center temperature generally agrees with the average of the axial direction data.

Mass loss data collected in several runs for the cylindrical particle appear with model predictions in Figure 7.

The shapes of the temperature histories illustrate the complexity of this large-particle pyrolysis process even in the absence of complications arising from surface oxidation and surrounding flames. The initial low center temperature is associated with vaporization, which occurs at subboiling temperatures under nearly all conditions. Experiments with more moist particles reported later illustrate more clearly the impacts of vaporization. After vaporization, particles heat up relatively
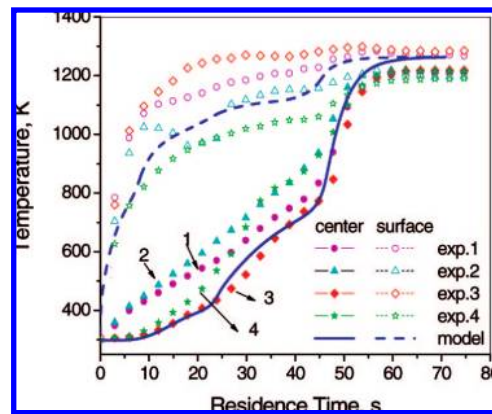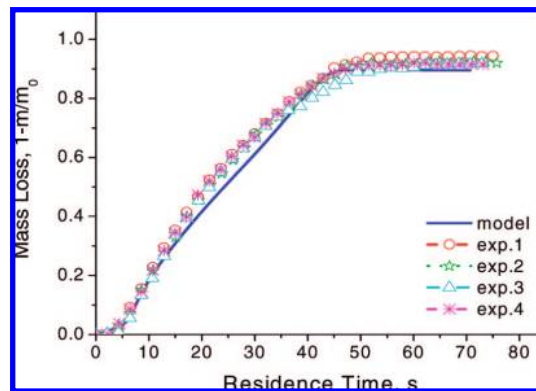
slowly, mainly because devolatilization reactions in outer layers of the particle generate significant gas velocities in the pores (commonly reaching 0.2 m/s), thereby impeding internal heat transfer. After devolatilization, particle temperature increases rapidly, mainly because the particle mass is greatly reduced relative to the early data by virtue of volatile losses but significantly because the internal heat transfer impediment from rapid outgassing also subsides. By contrast, the surface particle temperature increases rapidly and is less susceptible to slow heat transfer rates or even significant impacts from the blowing factor, in this case because radiation is the dominant heating mechanism. If convection were the primary heating mechanism, surface temperature heating rates would decrease by factors of up to 10 during rapid mass loss due to the outgassing effects. These processes result in temperature differences between the surface and the center of many hundreds of degrees Kelvin during particle heatup.

Particle Drying and Devolatilization. The drying model was further tested using wet particles with higher moisture content. Particle surface temperature and center temperature were measured with type K thermocouples in a cylinder particle with 40 wt % moisture (based on total wet particle mass) during drying and devolatilization. Similar to the previous experiments, particle center temperature measured in both axial and radial directions produced different results, with those in the axial direction more reliable. Results appear in Figure 8, which includes model predictions and data. Lines 1 and 2 indicate the center temperature measured in the radial direction, and lines 3 and 4 indicate the axial measurement. Both the model prediction and experimental data showed that the particle temperature first
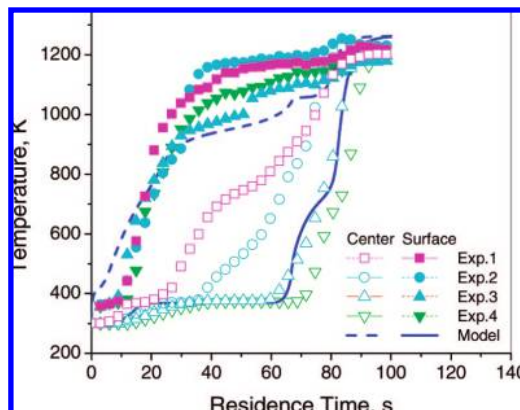
Figure 8. Temperature comparisons of a cylindrical particle during drying and pyrolysis in nitrogen (d_p = 9.5 mm, AR = 4.0, MC = 40 wt %, T_w = 1276 K, T_g = 1050 K).

Figure 9. Mass loss of a cylindrical particle during drying and pyrolysis in nitrogen (d_p = 9.5 mm, AR = 4.0, MC = 40 wt %, T_w = 1276 K, T_g = 1050 K).

Figure 10. Temperature profiles of a near-spherical wet particle during combustion in air (d_p = 9.5 mm, AR = 1.0, MC = 40 wt %, T_w = 1276 K, T_g = 1050 K).

rises to a constant value near but below the boiling point, with evaporation mainly occurring in this stage. Following drying, the particle temperature increases rapidly until biomass devolatilization slows the particle heating rate due to endothermic decomposition of biomass materials (minor effect) and the effect of rapid mass loss on the heat transfer coefficient, often called the blowing parameter (major effect if convection dominates the particle heatup). Once all biomass material converts to char, light gas, and tar, the residual char undergoes a rapid center temperature rise due to its lower mass (major effect), lower heat capacity (minor effect) and return of the blowing factor to near 1.

During most of the particle history, the predicted surface temperature is approximately 200 K below the average measured surface temperature. The predicted surface temperature depends primarily on radiative heating, convective heating, the impact of the blowing factor on heat transfer, and the rate and thermodynamics of water vaporization. As discussed later, the blowing factor in this radiation-dominated environment has little impact on the predictions. The thermodynamics of water vaporization are in little doubt, although the thermodynamics of the chemically adsorbed water losses are relatively uncertain. It is also possible that the reactions of the particle with its attendant changes in size and composition compromise the thermal contact between the surface thermocouple and the particle. There is no clear indication of whether the discrepancy arises from experimental artifacts or from uncertainties in emissivity and transport coefficients or other factors.

Figure 9 compares the predicted and measured mass loss data. The model does not predict the measured trend within its uncertainty though the predictions and measurements are in qualitative agreement. The disagreement is likely related to the temperature issues discussed above, including the nonuniformity of reactor temperature distribution. For a cylindrical particle horizontally oriented in the center of the reactor, its ends were exposed to higher temperature environment but the model applied an average bulk gas center temperature.

Particle Combustion. Figure 10 shows the temperature profiles of a wet, near-spherical particle with 40 wt % moisture content (based on the total wet particle mass) and aspect ratio of 1.0 during combustion.

A type B thermocouple provides temperature data for combustion experiments since the peak temperatures exceed the reliable range of type K thermocouples. The measured particle surface temperatures are not consistent with model prediction due to experimental artifacts associated with a shrinking particle. The surface contact is lost as the particle shrinks, and the bead
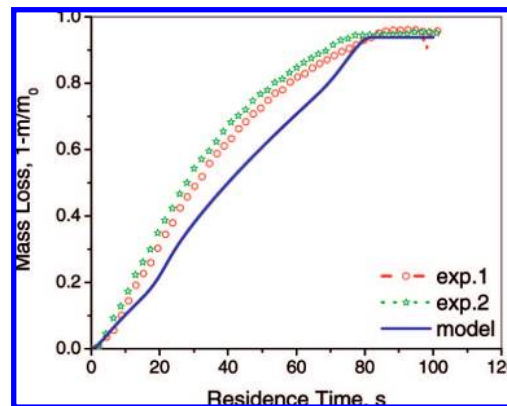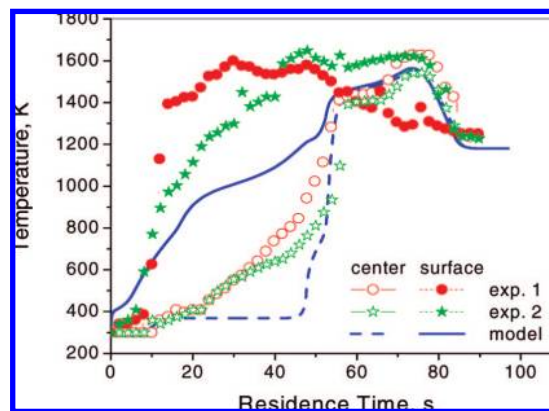
becomes exposed to the surrounding flame. The measured particle center temperatures appear to disagree with model predictions, though the disagreement arises primarily from thermocouple wire conduction. Both experimental data and model predictions show that during the char burning stage the particle temperature increases to a peak value and then declines dramatically. This supports theoretical descriptions of large-particle combustion mechanisms. Oxidizer diffusion rates primarily control combustion rates in char consumption, which proceeds largely with constant density and shrinking particle diameter. The char particle oxidation front finally reaches the center of the particle as particle size gets smaller with ash built up in the outer layer of the particle. The pseudo-steady-state combustion rate/temperature of the particle first increases then decreases with size due to changes in the relative importance of radiation losses, convection, and diffusion. Once the char is completely consumed, the particle (ash) cools rapidly to near the convective gas temperature, depending on the radiative environment.

The corresponding mass loss curves as functions of time appear in Figure 11. In this case, the data and predictions nearly overlap, though there remains a slight underprediction of the mass loss rate. This consistent underprediction could be partially caused by convective drag on the particle, making it appear less massive on the scale than it is.

For a low moisture content (6 wt %), near-spherical particle (d_p = 9.5 mm, AR = 1.0), the flame temperatures are measured with both thermocouple and camera pyrometry. A type B thermocouple mounted near the particle surface provides some measurements of the flame temperature surrounding the particle.
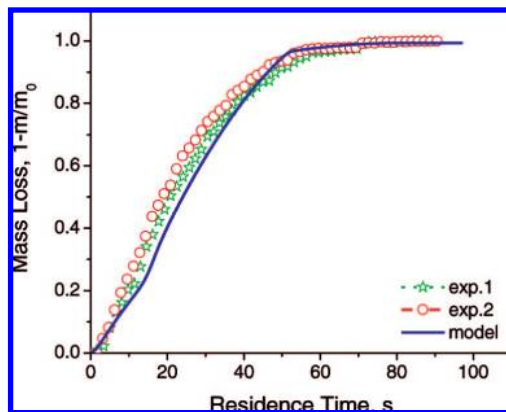
Figure 11. Mass loss of a near-spherical wet particle during combustion in air (d_p = 9.5 mm, AR = 1.0, MC = 40 wt %, T_w = 1276 K, T_g = 1050 K).
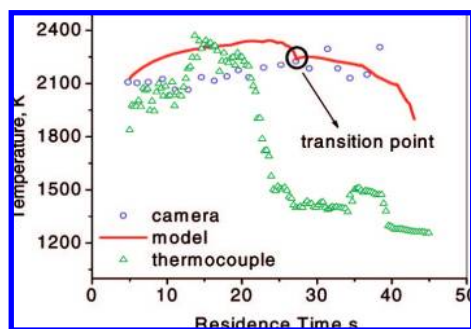

Figure 12. Flame temperature comparison during a near-spherical particle combustion in air (d_p = 9.5 mm, AR = 1.0, MC = 6 wt %, T_w = 1273 K, T_g = 1050 K).

The upper limit of a type B thermocouple is about 2100 K, and the thermocouple data above this value are not accurate, as shown in Figure 12. The flame temperature was also interpreted by the imaging pyrometer with gray-body emission assumption, where the results are combinations of flame and particle surface radiations. Both thermocouple and pyrometry data are compared with model predictions in Figure 12, where the flame receded away from the thermocouple after devolatilization. The thermocouple measurements fluctuate due to the turbulence and two-dimensional effects caused by the bulk gas convection, which is not captured in this one-dimensional model. In the camera pyrometry measurements, soot was assumed as gray-body emitter, although there is some spectral character to soot emission and the camera pyrometry measurements can be improved if spectral-dependent emissivity is applied in the calculation.[59] The model prediction of the flame indicates the transition of combustion from devolatilization stage to char burning stage, appearing in Figure 12. Results show that model predictions generally agree with both the camera-measured data and thermocouple data, and the difference is within measurements uncertainty.

This now-validated particle combustion model predicts the relative importance of effects of different factors such as temperature gradients, blowing, and flame reaction, as illustrated below.

Nonisothermal Effects. Both experimental data and model predictions showed that large temperature gradients exist in large biomass particles during combustion. An isothermal particle assumption incorrectly predicts both temperature and mass loss
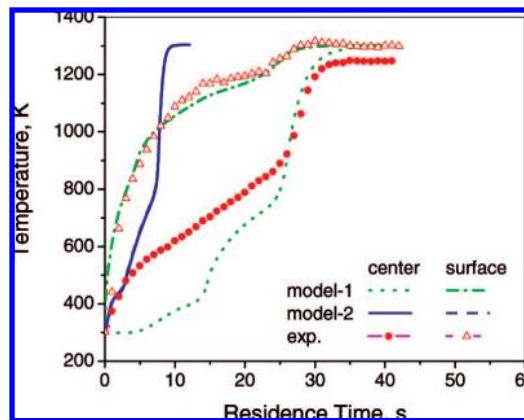
(59) Murphy, J. J.; Shaddix, C. R. Influence of scattering and probe-volume heterogeneity on soot measurements using optical pyrometry. *Combust. Flame* **2005**, *143* (1−2), 1−10.

Figure 13. Effects of temperature gradients on particle pyrolysis in nitrogen Nonisothermal assumption for model 1 and isothermal assumption for model 2 (d_p = 9.5 mm, AR = 1.0, MC = 6 wt %, T_w = 1273 K, T_g = 1050 K).
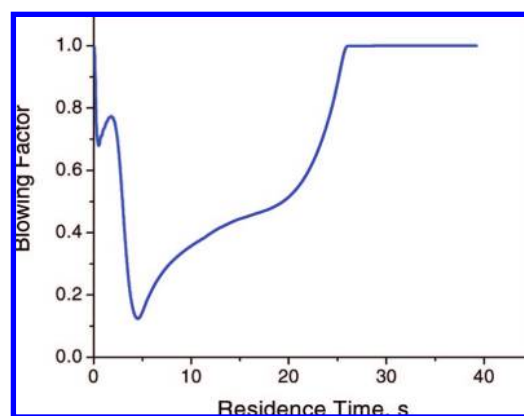

Figure 14. Blowing factor during particle pyrolysis process in nitrogen (d_p = 9.5 mm, AR = 1.0, MC = 6 wt %, T_w = 1273 K, T_g = 1050 K).

for large particles, as illustrated in Figure 13, where pyrolysis experimental data of a 9.5 mm dry, near-spherical particle are compared with model predictions with isothermal and nonisothermal assumptions. The model with isothermal assumptions predicts overall conversion rates approximately three times faster than the nonisothermal model, the latter being in good agreement with experimental data. In the isothermal prediction, the surface temperature, which controls the rate of convective and radiative heat transfer, is the same as the average particle temperature. The prediction with the temperature gradient indicates the surface temperature increases much faster than the average temperature, decreasing the average driving force for heat transfer and prolonging the reaction time of the particle. The difference between isothermal predictions and predictions with temperature gradients decreases with decreasing particle size, but the predicted conversion times do not become comparable (within 10%) until the size is less than 100 μm, which is much smaller than the average particle size used in commercial operation.

Effects of Blowing on Particle Temperature. During pyrolysis, the blowing factor of the 9.5 mm particle becomes as low as 0.1, as shown in Figure 14. This pronounced impact on heat transfer is not observed when radiation dominates particle heating, as illustrated by the predicted temperature profiles of a biomass particle in the single-particle reactor with and without blowing factor correction in Figure 15, where the particle heating history is nearly independent of the blowing effects correction. However, for environments dominated by convective heating,
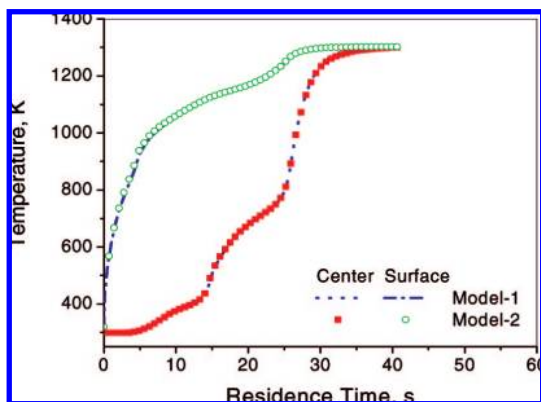
Figure 15. Particle temperature profile during particle pyrolysis in nitrogen with and without blowing factor correction when radiation dominates (model 1 with blowing factor correction and model 2 without blow factor correction; d_p = 9.5 mm, AR = 1.0, MC = 6 wt %, T_w = 1303 K, T_g = 1050 K).
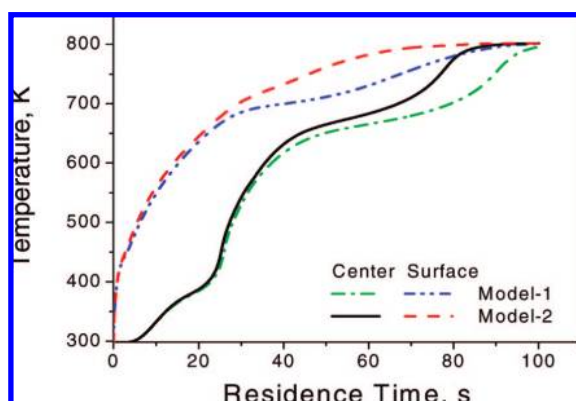

Figure 16. Effects of blowing factor on particle temperature during pyrolysis in nitrogen when convection dominates (Model-1 with blowing factor correction and model-2 without blow factor correction; d_p = 9.5 mm, AR = 1.0, MC = 6 wt %, T_w = 298 K, T_g = 1400 K).

Figure 17. Effects of flame on near-spherical particle temperature during combustion in air (model 1 stands for results without flame included, model 2 for those with flame included; d_p = 9.5 mm, AR = 1.0, MC = 6 wt %, T_w = 1273 K, T_g = 1050 K).

Figure 18. Particle radius, boundary layer thickness, and off-gas velocity during a wet particle combustion process in air (d_p = 9.5 mm, AR = 1.0, MC = 6 wt %, T_w = 1273 K, T_g = 1050 K).

the blowing factor has a major impact on overall heat transfer rates, and the blowing factor slows down the particle pyrolysis process by about 20%, as indicated in Figure 16.

Effects of Surrounding Flame during Particle Combustion. The current single-particle combustion model simulates the boundary layer and the flame formed around the particle surface in the boundary layer, as well as predicting the boundary layer thickness.

Figure 17 illustrates the effects of the boundary layer simulation and surrounding flame on the particle temperature profiles during combustion. Simulations both including and neglecting the surrounding flame appear in this graph. As expected, essentially no difference exists between the two simulations early in devolatilization (flame not yet ignited). Slight differences in the surface temperature start to appear during the late devolatilization stage and early oxidation stage of combustion, but the flame actually decreases the predicted surface temperature in this case. This counterintuitive decrease is associated with the flame consuming oxygen in the boundary layer that otherwise would have reacted with the particle. The relatively minor thermal feedback from the flame to the particle impacts the particle surface temperature less than the reduction in surface reaction associated with the decreased oxygen concentration. During the bulk of oxidation, the flame increases the predicted surface temperature by about 100 K. The modeled particle final temperatures differ from each other by about 20 K. This minor discrepancy arises from the method applied to
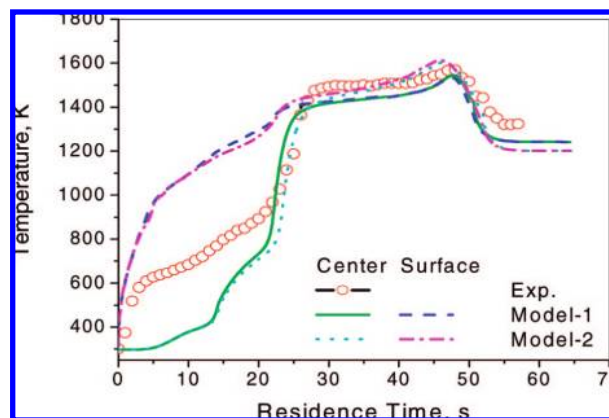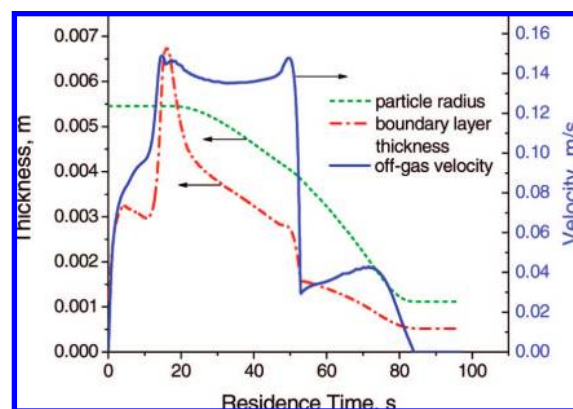
determine the boundary layer thickness. In the model including flame layer the boundary layer thickness is based on the linear heat and mass transfer correlations which were used in the model without flame layer. In the boundary layer, temperature distribution is not linear for a spherical coordinate and the tangent (slope) on the surface becomes greater than linear distribution. This increases the convection heat transfer in the boundary and hence decreases the particle surface temperature.

Model results also indicate that particle temperature becomes dramatically more uniform during char burning, although the flame feedback maintains a surface temperature greater than the center temperature, unlike theoretical predictions for particles with oxygen penetration but no flame feedback. These relatively subtle effects on flame temperatures are too small for accurate measurements by our techniques.

Generally speaking, nonisothermal effects will slow down the heat transfer (both radiation and convection) between the bulk gas and particle surface due to the decrease of temperature difference. Also for convection-dominated particle heat transfer, the blowing factor (which is caused by high mass transfer in the boundary layer) will dramatically reduce the heating rate to the particle. Surrounding flame affects the particle temperature mainly during the char burning stage.

The modeled particle radius, boundary layer thickness, and off-gas velocity as functions of residence time during drying, devolatilization, and char burning appear in Figure 18.

Although the three processes of drying, devolatilization, and char oxidation occur simultaneously for large particles such as the 11 mm poplar particle used in this investigation, they can

still be approximately identified from both experimental data and model predictions, as shown in Figures 10 and 18. Drying mainly finishes in the first 20 s followed by primary devolatilization that lasts about 30 s; char oxidation requires an additional 30 s. The modeling results also show that the particle shrinks slightly during drying and shrinks more rapidly during char burning.

The comparisons between experimental data and model predictions with different levels of complexity demonstrate that for biomass particle combustion a model with such a sophisticated structure is necessary, which takes particle shape, size, surface area, temperature and concentration gradients, and flame effects into account.

5. Conclusions

A relatively general purpose particle combustion model capable of simulating drying, recondensation, devolatilization, and char oxidation and gasification, and swelling/shrinking as well as gas-phase combustion surrounding biomass particles was developed to compare with original data. Comparisons were made of particle center and surface temperatures and overall mass loss. Model predictions included many additional features of biomass combustion less amenable to direct measurement.

The data and model developed in this investigation describe single-particle biomass combustion rates reasonably well. Generally, agreement within a few percent of the measured values is achieved, though in most cases there remain generally small but statistically signficant differences between predictions and measurements.

Isothermal spherical mathematical approximations for fuels that either originate in or form aspherical shapes during combustion poorly represent combustion behavior when particle size exceeds a few hundred microns. This includes a large fraction of the particles in both biomass and black liquor combustion. In particular, composition and temperature gradients in particles strongly influence the predicted and measured rates of temperature rise and combustion, with large particles reacting more slowly than is predicted from isothermal models.

Nomenclature

A = pre-exponential factor, s^{-1}; area, m^2
AR = aspect ratio
BLT = boundary layer thickness, m
C_p = heat capacity, $J\cdot kg^{-1}\cdot K^{-1}$
d = diameter, m
D_{eff} = effective diffusivity, $m^2\cdot s^{-1}$
D_{AB} = molecular diffusivity, $m^2\cdot s^{-1}$
D_K = Knudson diffusivity, $m^2\cdot s^{-1}$

E_i = activation energy, $J\cdot mol^{-1}$
h_f = heat transfer coefficient, $W\cdot m^{-1}\cdot K^{-1}$
h_m = mass transfer coefficient, $m\cdot s^{-1}$
$\hat{H}$ = enthalpy, $J\cdot kg^{-1}$
k = rate constant; devolatilization reaction = s^{-1}; heterogeneous reaction = $m\cdot s^{-1}$
K = thermal conductivity, $W/m\cdot s$
M = molecular weight, $kg\cdot kmol^{-1}$
M_W = gas average molecular weight, $kg\cdot kmol^{-1}$
n = shape factor
Nu = Nusselt number
p = pressure, Pa
Pr = Prandtl number
r = radius coordinate, m; reaction rate, $kg\cdot m^{-3}\cdot s^{-1}$
Re = Reynolds number
R/R_g = universal gas constant, $J\cdot mol^{-1}\cdot K^{-1}$
R_p = particle radius, m
R_{SA} = surface area ratio
t = time, s
S_a = particle specific surface area, $m^2\cdot m^{-3}$
SA = surface area, m^2
T = temperature, K
u = gas velocity, $m\cdot s^{-1}$
υ = volume, m^3
x = conversion
Y = mass fraction

Greek symbols
α = proportional factor
β = particle/droplet swelling/shrinking factor
ϵ = porosity
μ = viscosity, $Pa\cdot s$
η = permeability, Darcy
θ = blowing factor
ρ = density, $kg\cdot m^{-3}$
ΔH = heat of reaction, $J\cdot kg^{-1}$

Subscripts
0 = initial value or reference state
A = ash
B = biomass
C = char
con = conductivity
eq = equivalent
G = gas phase
G = light gas
HC = hydrocarbon
I = species or component in solid phase
J = species or component in gas phase
K = species or component in liquid phase
I = inert gas
M = moisture
P = particle
rad = radiation
V = water vapor
T = tar
w = wall

EF800006Z